Interplay between VSD, pore and membrane lipids in electromechanical coupling in HCN channels

Ahmad Elbahnsi[1]*, John Cowgill[1]*, Verena Burtscher[2], Linda Wedemann[1], Luise Zeckey[1], Baron Chanda[2] and Lucie Delemotte[1]

Affiliations

* These authors contributed equally.

1 Department of Applied Physics of Science for Life Laboratory, KTH Royal Institute of Technology, Sweden
2 Center for Investigation of Membrane Excitability Diseases, Department of Anesthesiology, Washington University School of Medicine, St Louis, MO, USA

Lead contact:
Lucie Delemotte.
E-mail: lucied@kth.se

Abstract

Hyperpolarized-activated and Cyclic Nucleotide-gated (HCN) channels are the only members of the voltage-gated ion channel superfamily in mammals that open upon hyperpolarization, conferring them pacemaker properties that are instrumental for rhythmic firing of cardiac and neuronal cells. Activation of their voltage-sensor domains (VSD) upon hyperpolarization occurs through a downward movement of the S4 helix bearing the gating charges, which triggers a break in the alpha-helical hydrogen bonding pattern at the level of a conserved Serine residue. Previous structural and molecular simulation studies had however failed to capture pore opening that should be triggered by VSD activation, presumably because of a low VSD/pore electromechanical coupling efficiency and the limited timescales accessible to such techniques. Here, we have used advanced modeling strategies, including enhanced sampling molecular dynamics simulations exploiting sequence/structure conservation principles in non-domain swapped voltage-gated ion channels to trigger pore gating and characterize electromechanical coupling in HCN1. We propose that the coupling mechanism involves the reorganization of the interfaces between the VSD helices, in particular S4, and the pore helices S5 and S6, subtly shifting the balance between hydrophobic and hydrophilic interactions in a "domino effect" during activation and gating in this region. Remarkably, our simulations reveal state-dependent occupancy of lipid molecules at this emergent coupling interface suggesting a key role of lipids in hyperpolarization-dependent gating. Our model provides a rationale for previous observations and a mechanism for regulation of HCN channels by the lipidic components of the membrane.

Introduction

Hyperpolarized-activated and Cyclic Nucleotide-gated (HCN) channels, also known as pacemaker channels, are non-selective cation channels located at the plasma membrane of pacemaker cells in the heart and brain. These channels are crucial to control the rhythmic activity in many cell-types and further regulate cellular excitability in a wide range of electrically excitable cells (Brown et al., 1979; Santoro et al., 1998). The ability to drive rhythmically firing action potentials stems from the unusual and characteristic channel activation under membrane hyperpolarization. Given their ubiquity in excitable organs and unique role in electrical signaling, HCN channels have been implicated in a variety of diseases (e.g. heart arrhythmias, epilepsies and neuropathic pain) and are considered as promising targets for the development of novel drugs (Benarroch, 2013; Biel et al., 2009; Bleakley et al., 2021; DiFrancesco and DiFrancesco, 2015; DiFrancesco et al., 2019; Oyrer et al., 2019; Tanguay et al., 2019).

HCN channels are members of the voltage-gated ion channel (VGIC) superfamily, and as such form tetrameric assemblies around a central pore that opens and closes in response to changes in the transmembrane voltage. Each monomer is composed of six transmembrane helices divided in two domains: the voltage-sensing domain (VSD) is a four-helical bundle formed by the first four helices (S1 to S4) (Long et al., 2005) while the pore domain is formed by tetramerization of the final two helices (S5 and S6) around the symmetry axis (Lu et al., 2001).

HCN and other VGICs are allosteric systems where movement of gating charges in the VSD upon changes in electric field governs opening and closing of the pore gate located >10A away at the C-terminus of the S6 helix in a process known as electromechanical coupling (Blunck and Batulan, 2012; Long et al., 2005). Interestingly, the polarity of the coupling in HCN channels is inverted relative to nearly all other VGICs; HCN channels are opened by the downward movement of the gating charges during hyperpolarization whereas most other channels are closed (Männikkö et al., 2002). Inverted electromechanical coupling is central to the role of HCN channels in pacemaking, but the molecular mechanisms underlying inverted coupling have remained elusive.

The first high-resolution structures of HCN1 revealed that, unlike canonical VGICs, HCN channels adopt a non-domain swapped architecture where the VSD packs against the pore domain of the same subunit (Lee and MacKinnon, 2017). This unusual fold is not unique to HCN channels but rather is characteristic of the subfamily of channels containing a C-terminal cyclic nucleotide binding domain (CNBD) connected to the pore via the C-linker (James and Zagotta, 2018). Other members of this family include the depolarization-activated KCNH subfamily, such

as ether-á-go-go (EAG) and human EAG related gene (hERG), and voltage-insensitive cyclic nucleotide gated (CNG) channels (Whicher and MacKinnon, 2016; Wang and MacKinnon, 2017; Li et al., 2017).

A flood of new structures in addition to the functional and computational studies they fueled have revealed new atomistic details of voltage sensing and pore gating for numerous members of the CNBD family including HCN channels. HCN1 structures were obtained in resting and activated conformations of the VSD but the pore remained closed in both models (Lee and MacKinnon, 2017, 2019). The model for VSD activation from these structures agrees with predictions from cysteine accessibility (Bell et al., 2004), patch clamp fluorometry (Dai and Zagotta, 2017), and molecular dynamics (MD) simulations (Kasimova et al., 2019). Furthermore structures of HCN4 have been resolved in both the closed and open state but in both cases, the VSD is in the resting conformation (Saponaro et al., 2021). Together, the HCN1 and HCN4 structures represent three out of the four states in a classical allosteric model of channel gating; the resting-closed, activated-closed, and resting-open conformations. The missing activated-open state is central to understanding the electromechanical coupling mechanism in the HCN family.

Unfortunately, even with a structure of the activated-open state in hand, the weak nature of the VSD-pore coupling in these channels limits our ability to make inferences about the coupling pathway. The experimentally measured coupling energy of only 3-4.5 kcal/mol indicates that activation of all four voltage sensors only increases the stability of the open pore relative to the closed pore by roughly one hydrogen bond (Ryu and Yellen, 2012). Given this weak coupling, it is important to not only examine the static structures themselves, but also the structural ensembles and dynamics of the interactions comprising each state.

In this work, we use a stepwise approach to build an understanding of the electromechanical coupling pathway in HCN1. First, we characterize state-specific interactions by analyzing MD simulations of existing cryoEM structures under equilibrium and activating conditions. We then use a small subset of the interactions likely to stabilize the activated-open channel in enhanced sampling simulations to drive the electromechanical coupling process. Gathering the results, we propose an electromechanical coupling model that relies on a fine-tuned balance between hydrophilic and hydrophobic interactions at the voltage-sensor and pore domain interface. Notably, by characterizing the state-dependent interactions between lipids and the channel domains, we propose an important role for amphiphilic membrane components, rationalizing the effect of changes in membrane composition on the function of this channel.

Results

State-dependent interactions between VSD and pore domain in HCN1 models

In the current model for VSD activation in HCN channels, hyperpolarization triggers a downward motion of S4 coupled to a kinking of the helix at S272. This breaks S4 into two sub-helices with the lower segment becoming almost parallel to the membrane (Figure 1A,C). This non-canonical voltage sensing mechanism is supported by both experimental and computational studies combined with the cryoEM structure of the activated state stabilized by cysteine cross-linking (Lee and MacKinnon, 2017, 2019; Bell et al., 2004; Dai and Zagotta, 2017; Kasimova et al., 2019). An additional structure was resolved for the functionally locked-open Y289D mutant, in which the gating charges are in a resting state and the pore is closed, but the lower S5 helix swivels away from S6 relative to the position in the wild-type channel in a manner similar to the activated state structure (Figure 1B) (Lee and MacKinnon, 2019). While the mechanism of VSD activation is well established, the mechanism by which this voltage sensor movement triggers pore opening remains poorly understood as the activated-open state of HCN has not been determined.

The movement of the lower half of the S4 helix upon activation drastically alters the interaction networks between the VSD, N-terminal HCN domain, and pore (Figure 1A-C). To help understand which state-dependent interactions stabilize each of the conformations observed in cryoEM, we carried out 1µs-MD simulations of the resting, activated, and Y289D mutant conformations under equilibrium conditions (0 mV). These simulations highlighted W281 as a potentially critical residue in gating given the extensive state-dependent contacts maintained from the resting, activated, and Y289D mutant starting systems (Figure 1G).

In the resting state, W281 is facing S1 and nestled in a hydrophobic cavity formed at the interface between S4, S1 and the HCN domain (Figure 1D) and remains stably bound at this position throughout the simulation (Figure 1G, purple bars). This conformation of W281 is stabilized by extensive hydrophobic interactions with S1 and the HCN domain in addition to an electrostatic contact with S1 for >50% of the simulation time (Figure 1G).

In the activated state, the intracellular S1-S4-S5 region becomes much less compact and W281 is pulled out of the hydrophobic cavity, disrupting all interactions with S1 (Figure 1F). A new interaction with the pore domain is formed via V296 in S5 but the overall protein contact of W281

is significantly reduced in the activated state. As a result, W281 primarily interacts with lipid (POPC) in the activated state through hydrophobic and electrostatic contacts.

The side chain orientation and contacts formed by W281 in the Y289D mutant retain aspects of both the resting and activated state (Figure 1E). While W281 remains close to S1, the interaction network with S1 is significantly altered relative to the resting state. Furthermore, the strong interaction with the HCN domain enclosing W281 in a hydrophobic cavity in the resting state is disrupted in the mutant. These differences stem from the rotation W281 to an orientation more similar to the activated state of the VSD. Rotation of W281 enables increased contacts with lipids and the pore domain similar to the activated state but interaction with S5 occurs via N300 in addition to the V296 contact observed in the activated state.

As a result of the mixed set of W281 contacts shared with the resting and activated states, the structure of the Y289D mutant can be described as an "intermediate state" conformation for VSD activation. The rotation W281 resembles the activated state, but the interactions with S1 retain the compact nature of the S1-S4-S5 region similar to the resting state. This configuration is quite interesting as the Y289D mutant retains many characteristics of the VSD-pore interactions of the activated state despite the fact that the gating charges are in their resting position and S4 does not adopt the characteristic bend associated with voltage sensor activation.
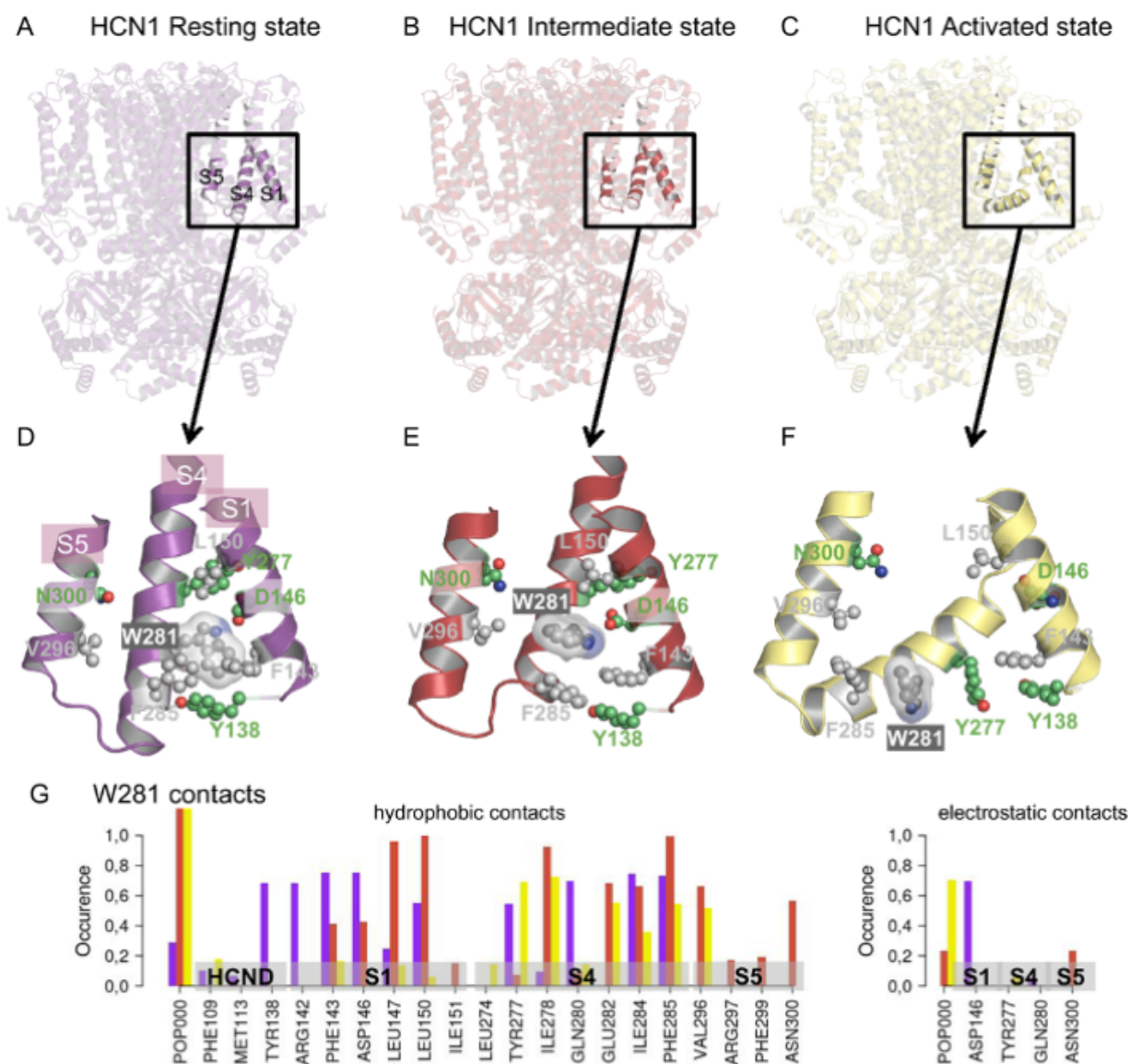
Figure 1: Position and contact network of W281.

The 3 cryo-EM structures of the resting (A - PDB ID 5U6P), intermediate (B - PDB ID 6UQG) and activated (C - PDB ID 6UQF) states of hHCN1, shown in purple, red and yellow, respectively, were investigated by equilibrium MD simulations. The position of W281 is highlighted in ball/stick and transparent surface and surrounding residues are shown in ball and stick in the resting (D), intermediate (E) and activated (F) conformations. (G) Contact occurrence between W281 and nearby residues and lipid molecules along 1µs-long MD simulations.

Dynamics of VSD-pore interactions upon voltage sensor activation

The state-dependent VSD-pore interactions correlated with rotation of the C-terminus of S4 at W281 outlined above hint at a possible functional role in electromechanical coupling. To gain insight into the evolution of these state-dependent interactions over the course of channel

activation, we simulated the resting state under a hyperpolarizing transmembrane potential. We used three new strategies in an attempt to further accelerate VSD activation compared to our previous study in hopes of driving the channel to the activated-open state. First, we started from the cAMP-bound configuration of CNBD, which has previously been shown to allosterically promote both pore opening and VSD activation (Wu et al., 2011; Kusch et al., 2010). Next, we increased the magnitude of the membrane potential to -1 V (compared to -550 mV previously used). This should reduce the time constant for activation from 23 microseconds to 3 microseconds based on our previous kinetic analysis (Kasimova et al., 2019). Finally, we simulated an additional system lacking the HCN-domain (called hereafter HCND-less system), which has previously been suggested to inhibit VSD activation. This is consistent with our results above where the HCN domain acts as a lid enclosing W281 in a hydrophobic cavity in the resting state.

In the intact system, full activation occurs in only one VSD as marked by movement of R267 past the charge transfer center (Figure 2 - Figure supplement 1A). Partial activation as seen by movement of R270 past the charge transfer center occurs in one subunit while the remaining two VSDs show little to no displacement. In the subunits showing full or partial activation, S4 adopts the characteristic bend associated with channel activation observed in our previous simulations and the cryoEM structure of the cadmium-crosslinked activated state (Figure 2 - Figure supplement 1A). This suggests that the activation mechanism is preserved despite the high magnitude of transmembrane potential used. The incomplete activation of the voltage sensors in this system is not surprising given the length of the simulation (1 microsecond) compared to the predicted time constant for activation (3 microseconds).

For the HCND-less system, one VSD undergoes full activation while the remaining three undergo partial activation over the course of a 750 ns simulation (Figure 2 - Figure supplement 1B). This is consistent with an accelerated voltage sensor activation compared to the intact system expected by relieving inhibition of activation provided by the HCN domain. However, the wider distribution of bending angles in S4 for the system lacking the HCN domain indicates that the HCN domain may also contribute to stabilizing the activated state of S4 (Figure 2 - Figure supplement 1B and 2F).

During VSD activation, downward movement of the gating charges and bending of S4 is correlated with rotation of the C-terminus of S4, pointing W281 toward the lipid interface (Figure 2 - Figure supplement 1, 2C and 2F). In subunits undergoing complete activation, a more complete rotation of the C-terminus of S4 results in formation of a hydrogen bond between W281 and N300 that was observed in the Y289D mutant above (Figure 2 A-B, D-E, Figure 2 - Figure

supplement 2A,D). Interestingly, swapping these two residues inverts the gating polarity in the related spHCN channel (W355N/N370W in spHCN numbering). The proposed basis of this inverted coupling was a similar rotation of the lower S4 helix as we observed, but driven by introduction of a hydrophobic mismatch of the mutations rather than activation of the voltage sensor (Ramentol et al., 2020).

In our simulations of VSD activation, rotation of W281 is accompanied by an increase of the hydrophobic contact area at the lower S4/S5 interface with little change to the electrostatic interactions (Figures 2G, Figure 2 - Figure supplement 2B,E). On the other hand, analysis of the lower S4-S1 interface showed a decrease of the hydrophobic contacts between S4 and S1 in most (7 out of 8) subunits (Figure 2 - Figure supplement 2C,F). This suggests that separation of the S1/S4 interface is one of the first steps towards release of W281 from the S1/S4/HCN domain hydrophobic pocket and enabling rotation of the C-terminus of S4.

The combined bending and rotation of the lower S4 accompanies displacement of S1 away from S4 and exposes the VSD-pore interface to the lipid bilayer. As a result, an increased number of contacts between lipid tails and hydrophobic residues on S4 and S5 accompanies VSD activation (Figures 2I and Figure 2 - Figure supplement 3). The average number of POPC carbon atoms in contact with the lower S4/S5 interface is ~24±7 in the resting state versus ~40±7 in the activated state equilibrium simulation. This increase in lipidic contact upon activation is preserved whether the HCN domain is present or absent. Thus, lipid tails preferentially contact the VSD/pore interface in the activated state of the voltage sensor, indicating lipid tails may play a role in electromechanical coupling in HCN1. This may help reconcile the fact that the cryoEM structure of HCN1 with an activated voltage sensor as well as the Y289D mutant in detergent remained closed despite functional evidence suggesting that these channels should remain open at 0 mV (Lee and MacKinnon, 2019).

Despite the combination of three strategies to accelerate activation, the pore gate remained shut throughout these simulations. This is unsurprising given the slow intrinsic gating of the pore and the weak electromechanical coupling in the HCN family. Even in the presence of four activated voltage sensors, the closed to open pore transition for HCN1 has a time constant of ~100 ms based on allosteric models of channel gating (Altomare et al., 2001). Consequently, the pore opening process is far outside the current range of unbiased MD simulations for HCN1. We thus set out to further analyze state-dependent interactions in an attempt to pinpoint those that may help favor pore opening, to then be able to use them in enhanced sampling simulations.
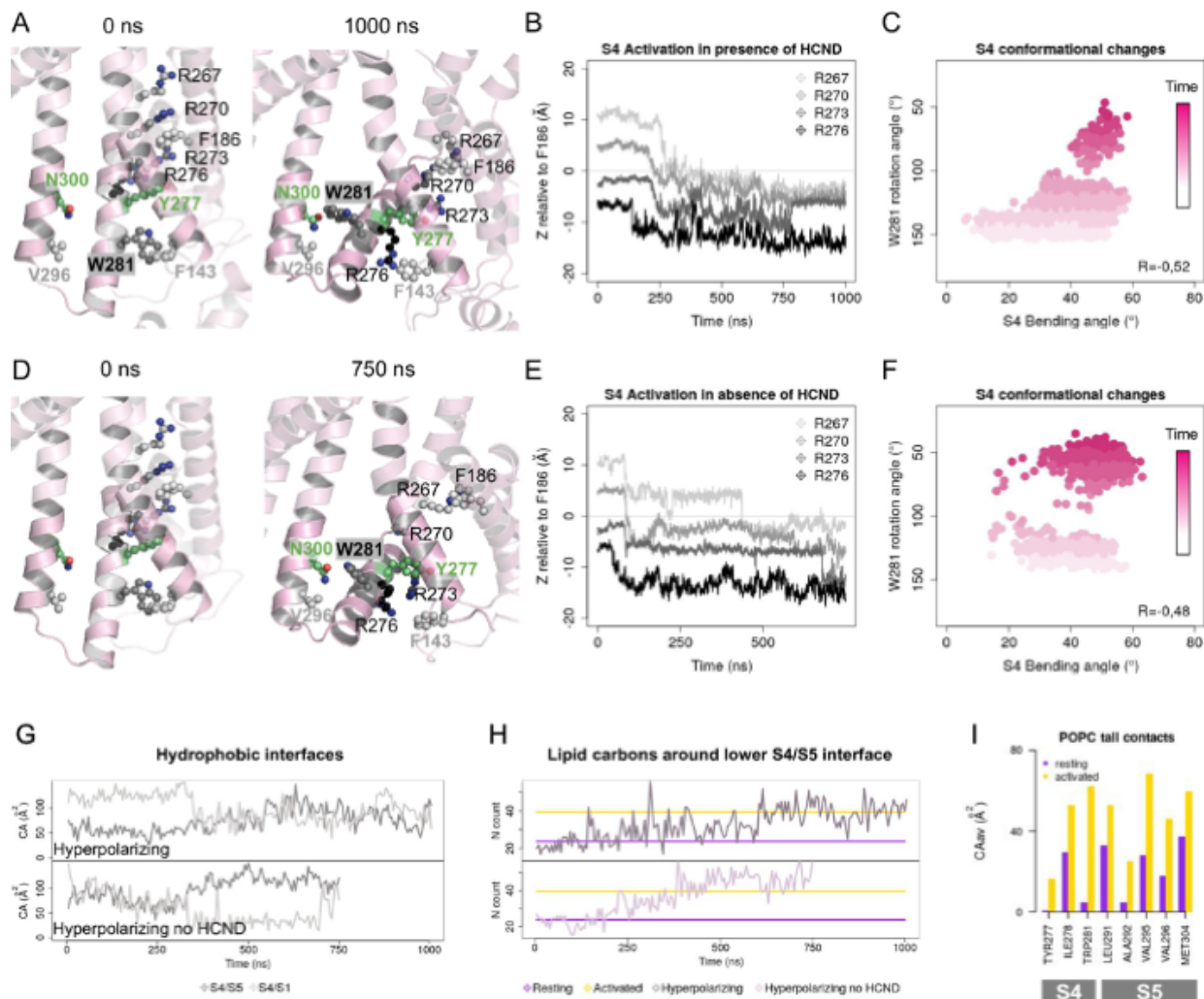
Figure 2: HCN1 activation induces an increase of the lower S4/S5 - lipids hydrophobic interfaces.

(A, D) First and last snapshots of VSDs extracted from activating simulations of intact (panel A, subunit D) or HCND-less system (panel D, subunit A). The gating charges and residues W281, Y277 (S4), N300 (S5) and F143 (S1) are highlighted using ball and stick representation. (B, E) Downward displacement of the gating charges with respect to the charge transfer center F186 during the activation of S4 in subunit D (panel B, intact HCN1 model) and subunit A (panel E, HCND-less HCN1 model) during activating simulations. (C,F) Correlation between the S4 bending angle and the rotation of W281 in subunit D (panel C, intact HCN1 model) and subunit A (panel F, HCND-less HCN1 model) during activating simulations. The time evolution is represented by a color gradient, from white/light pink to dark pink. (G) Evolution of the S4/S5 and S4/S1 hydrophobic interfaces (contact areas) along activating simulations of HCN1 in presence (subunit D, top box) or absence (subunit A, bottom box) of the HCN domain. (H) Evolution of the number of lipid carbon atoms, N, in contact with hydrophobic residues from the lower S4/S5 interface along activating simulations of HCN1 in presence and absence of HCN domain are shown for subunit D in brown (top box) and for subunit A in light purple (bottom box), respectively. N count values for the resting and activated states were averaged for the four subunits from the equilibrium simulations and are displayed as purple and yellow horizontal lines, respectively. (I) Contact area between lipid tails and residues on the lower S4/S5 interface, averaged over the four subunits and over the simulation time, in the resting (purple) and activated (yellow) states
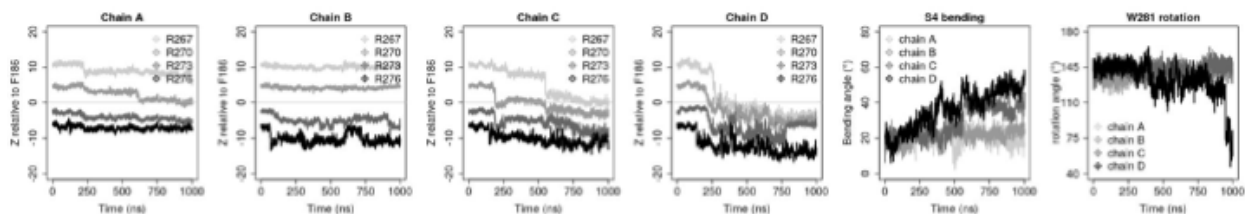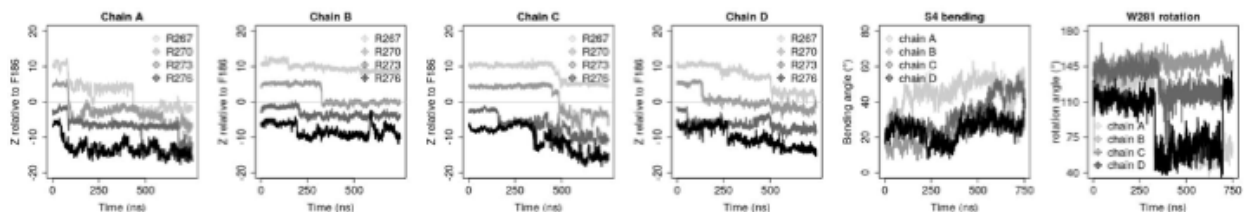
Figure 2 - Figure supplement 1: S4 activation of HCN1 channels

S4 displacement in simulations of the intact (A, 1 μs) or in the HCND-less system (B, 750 ns). In both panels, the first four columns represent the gating charges (R267, R270, R273 and R276 colored from light gray to black) movement with respect to the charge transfer center (F186, z=0) for the four protein chains (chains A, B, C and D). The last two columns show the evolution of the bending angle of S4 (defined as the angle between segments encompassing residues 252-272 and 272-289) and the rotation angle of W281 (defined as the angle between atoms Cα-V296 (on S5), Cα-W281 and CE2-W281 (on S4)). The four monomers, chains A, B, C and D are colored from light gray to black.
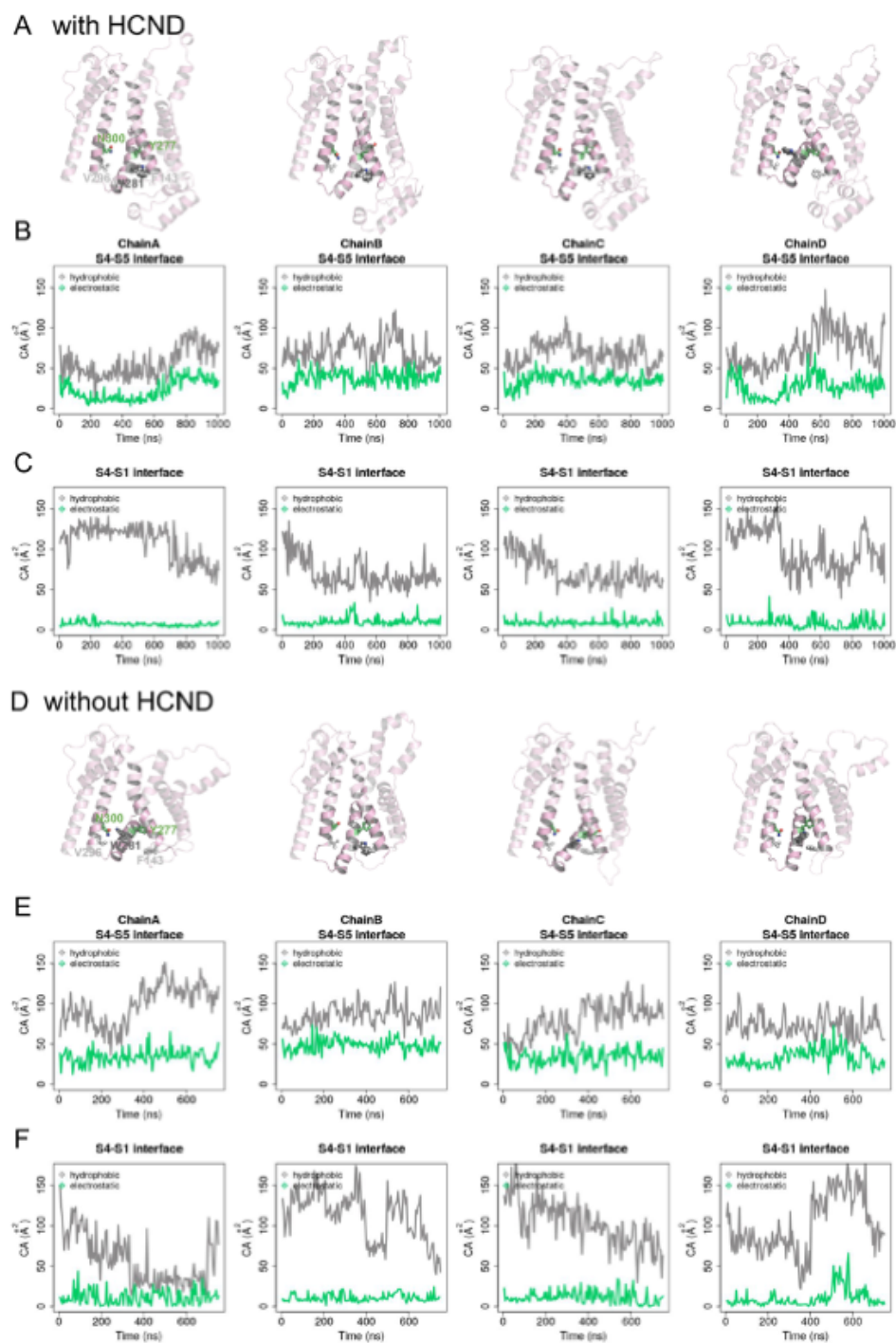
Figure 2 - Figure supplement 2: Evolution of the S4/S5 and S4/S1 interfaces in activating MD simulations of intact (A) and in HCND-less HCN1 models (B).

Each column represents a different subunit. First row: last snapshot from Hyperpolarizing EF-simulation showing the position of W281 and Y277 with respect to F143 and N300. Second row: hydrophobic (gray) and electrostatic (green) contact areas measured between the innermost parts of S4 (residues 277-289) and S5 (residues 290-305) as a function of simulation time. Third row: hydrophobic (gray) and electrostatic

(green) contact areas measured between the bottom parts of S4 (res 277-279) and S1 (res 139-150) as a function of simulation time.
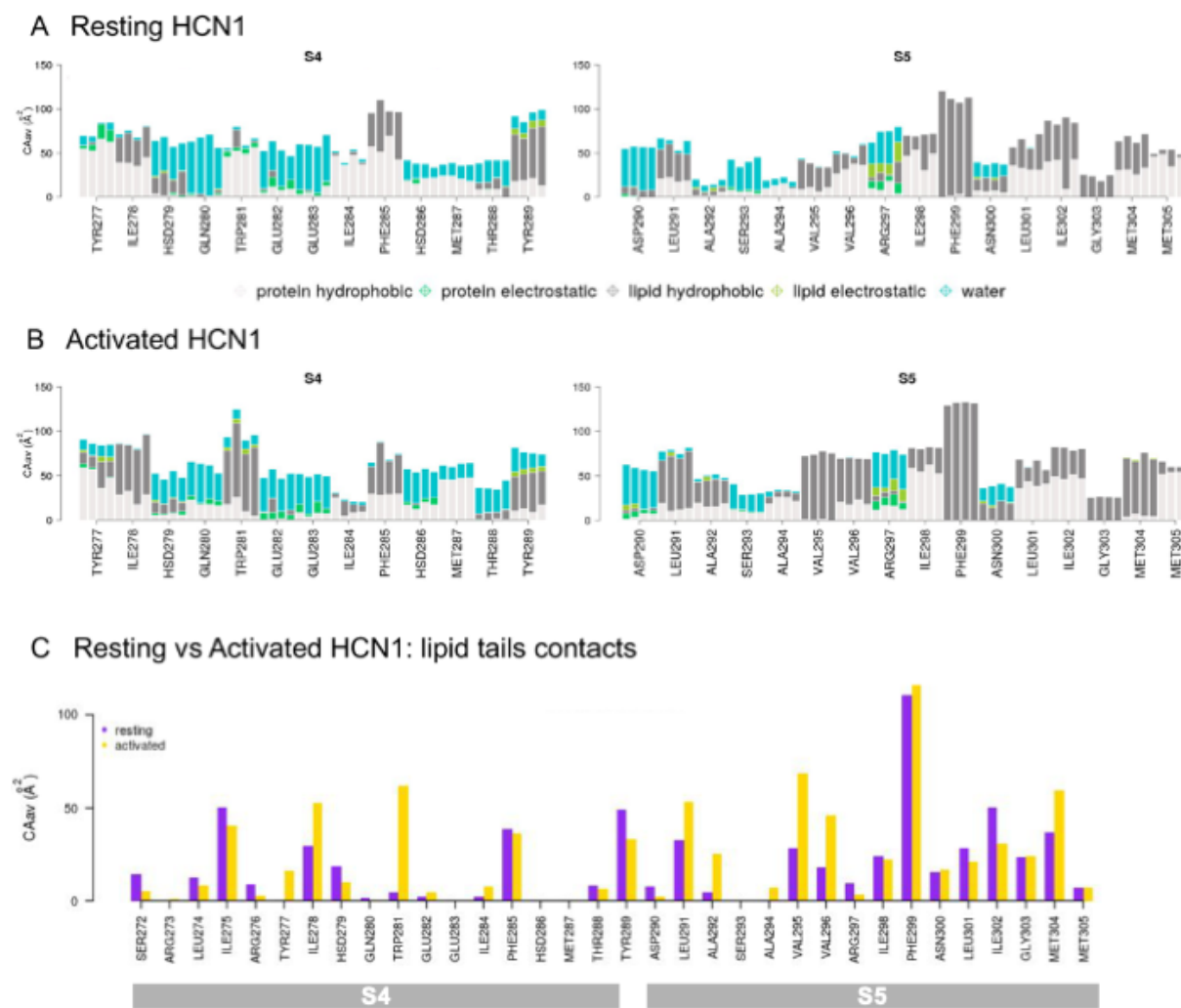

Figure 2 - Figure supplement 3: Hydrophobic and electrostatic interactions in the lower S4/S5 region are state-dependent.

Average contact areas between each residue/subunit from the lower S4 (left) and S5 (right) and surrounding hydrophobic (light gray) and hydrophilic (spring green) protein residues, lipid tails (dark gray) and headgroups (light green), and water molecules (turquoise) inthe resting (panel A) and activated (panel B) states equilibrium MD simulations (1 μs). C) Contact area between lower S4/S5 protein residues and lipid tails averaged over the 4 subunits and over the simulation time, in the resting (purple) and activated (yellow) states.

Displacement of S5 during VSD activation alters interaction between S4-S5 linker and C-linker

As a result of the bending and rotation of S4 during VSD activation, the N-terminal end of S5 is displaced relative to the resting state conformation in a movement that was previously observed in MD simulations and cryoEM structures. Interestingly, the C-terminus of S5 is similarly displaced in the Y289D mutant cryoEM structure despite lack of VSD activation in this channel (Figure 3A). These tilted conformations of the S5 helix are also observed in open channel structures of related CNBD family channels like hERG and TAX-4 ((Wang and MacKinnon, 2017; Zheng et al., 2020). Furthermore, this region of S5 directly contacts the S6 helix near the activation gate, thus the tilting movement of S5 following VSD activation was proposed as a critical step in the electromechanical coupling of HCN1 (Lee and MacKinnon, 2019; Kasimova et al., 2019).

In our simulations of the resting, activated, and intermediate (Y289D) structures above, we noted that tilting of S5 also alters the interaction network between the S4-S5 linker and the C-linker of the channel (Figure 3B). The C-linker directly connects the CNBD to the S6 activation gate and has previously been identified to play a role in electromechanical coupling based on numerous functional studies (Dai and Zagotta, 2017), therefore we suspected these activation-induced interactions may help drive channel opening.

The interaction between D290 of the S4-S5 linker and K412 of the C-linker is of particular interest given the clear state-specificity to both the active and intermediate states. The absence of this interaction in the resting state stems in part from the large distance between the positions of the backbones of these residues (Figure 3B). The tilting of S5 caused by activation or the Y289D mutation brings the D290-K412 positions in close proximity and enables stable salt bridge formation.

Interestingly, the D290-K412 distance in the original model of the activated VSD-closed pore conformation is close to the distance observed in the resting state structure. However, this distance decreases rapidly in the first few picoseconds of simulations and the resulting interaction remains stable for the majority of the trajectory (Figure 3C). Thus we hypothesize this interaction is involved in coupling VSD movement to gate opening through the C-linker.

Given that this interaction was not observed in the cryoEM structure of the activated VSD, we sought to experimentally validate the D290-K412 interaction in the activated-open state of the channel. Cysteine-crossbridging has been a successful approach to probe state-dependent interactions in HCN channels (Rothberg et al., 2003; Lee and MacKinnon, 2019). In this technique, pairs of residues are mutated to cysteine and then exposed to cadmium, which will

form high-affinity bonds between the thiolate groups provided the distance between residues is in the range of 6-8 angstroms. If the suspected interaction is state-specific, it will "lock" the channel in the corresponding functional state.

The HEK cells expressing D290C-K412C double mutant in the absence of cadmium conduct a relatively high basal current at depolarized potentials compared to the HCN1-EM parent constructs (Figure 3 - Figure supplement 1A). Much of this basal current can be blocked by application of external cesium chloride indicating the D290C-K412C does not fully close even in the absence of applied cadmium (Figure 3 - Figure supplement 1B,C). However, in HEK cells patched with 100 uM cadmium chloride in the pipette, the basal conductance increases substantially to 0.77 +/- 0.7 compared to 0.44 +/- 0.4 in the absence of cadmium (Figure 3D). Furthermore, the voltage dependence of activation shifts by 60 mV to more positive potentials (Figure 3D). The combined increase in the basal current amplitude and rightward shift in the voltage-dependence of activation strongly indicates that crossbridging these positions preferentially stabilizes the open state, in agreement with our hypothesis that the D290-K412 interaction promotes channel opening.
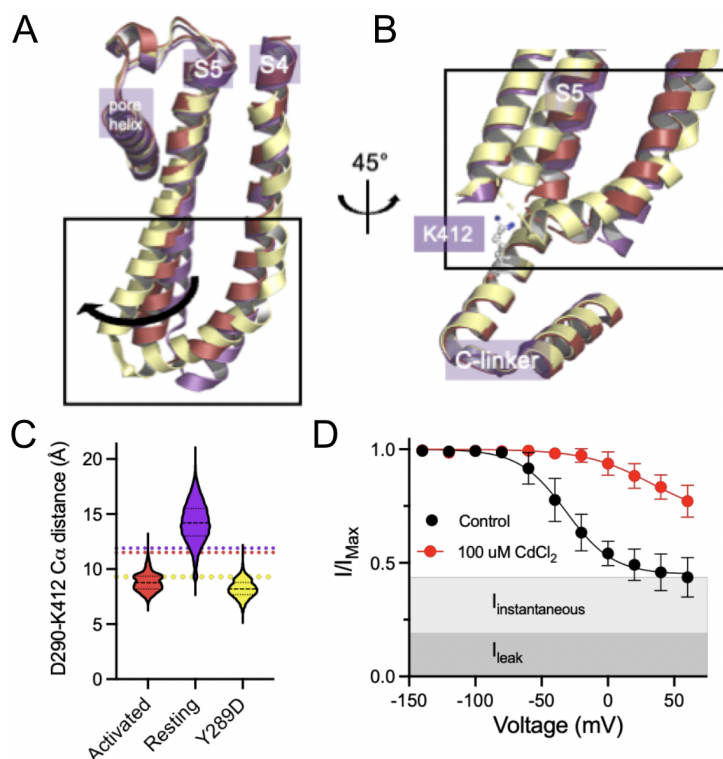

Figure 3: Structural comparison of the S4/S5 linker and C-linker regions.

(A) Structural comparison of the S4-S6 region of the resting (5U6P - purple), intermediate (6UQG - red) and activated (6UQF-yellow) states of hHCN1. Alignment was performed on the entire structure. (B)

Structural comparison of the S4/S5 linker and C-linker regions of the resting, intermediate and activated states of hHCN1. Residue K412 of the C-linker is shown as grey spheres. (C) D290-K412 distance distribution in simulations of the resting, intermediate and activated states. Dashed lines represent distances from the starting cryoEM structures of the same color. (D) Peak tail current versus voltage plot for whole-cell recordings from HEK cells expressing HCN1 D290C/K412C with (red) or without (black) 100 uM $CdCl_2$ in the patch pipette. Light shaded region indicates the average fraction of baseline current that is blockable by CsCl while dark shaded region indicates average fraction of baseline current that was not blockable by CsCl. Error bars represent SEM for n=5 independent cells for each condition.
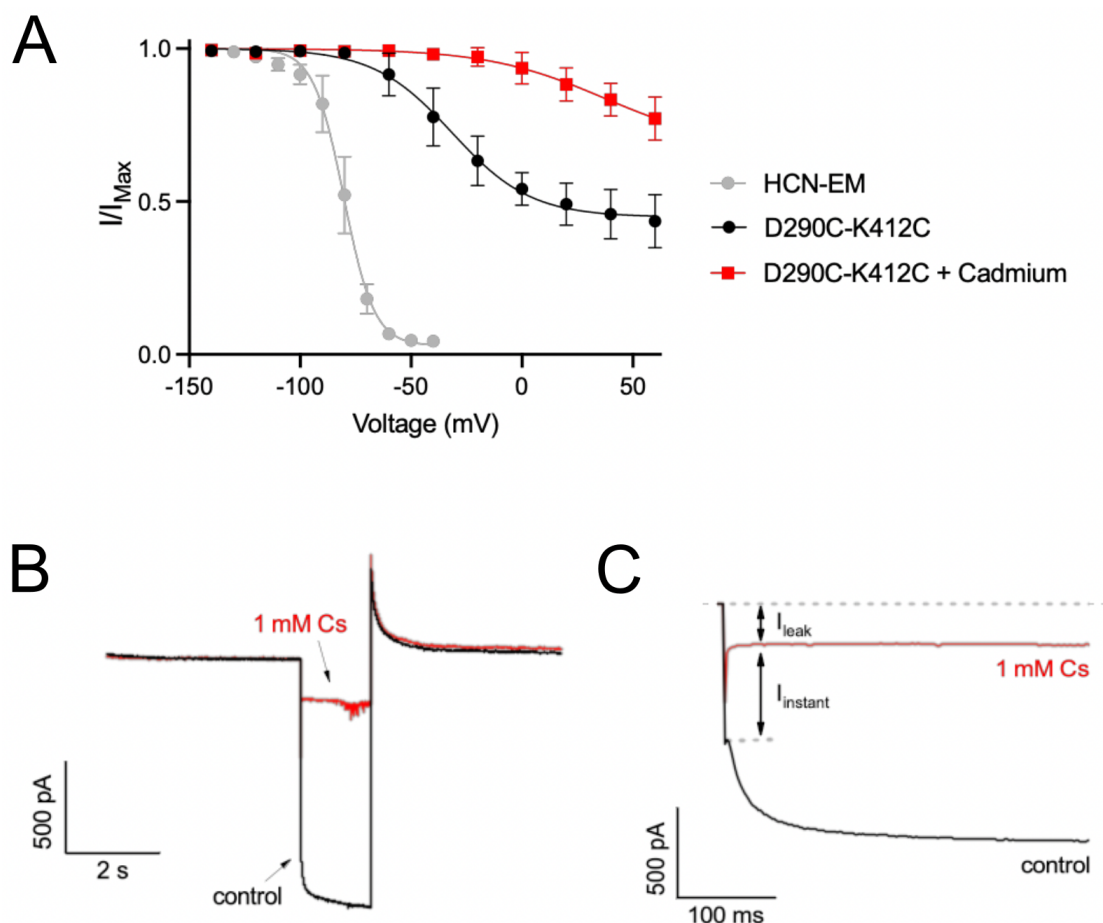

Figure 3 - Figure supplement 1: S6 deformation within the intracellular gate.

(A) Comparison of the relative peak tail current versus voltage relationships for HCN1-EM and the D290C-K412C double mutant with (red) and without (black) cadmium chloride in the patch pipette. Error bars represent SEM for n=5 independent cells for each condition. (B) Example of cesium blockage and residual leak current from cells expressing the D290C-K412C mutant. Currents are elicited from the same cell from test pulses to -140 mV with (red) and without (black) 1mM CsCl present in the bath solution. (C) Same as (B) showing just the test pulse to highlight the lack of time-dependence to the "instantaneous" current component ($I_{instant}$).

Modeling the open state of HCN1

In all of our simulations described previously and above, the S6 activation gate remained tightly closed and dehydrated for the entirety of the simulation. To gain insights into gating transitions of the HCN1 pore, we turned to the available structures in the CNBD channel family for which representative structures have been solved in closed and open states.

Comparing the open structure of hERG with the closed structure of the closely related rEAG channel, Wang et al. noted that opening of KCNH channels stems from bending of the S6 helix at a conserved glycine hinge (Wang and MacKinnon, 2017). Closer examination of these structures reveals an α to π helix transition directly adjacent to the glycine hinge (Figure 4 - Figure supplement 1A). This π-helical conformation is stable for the majority microsecond-long simulation in the hERG open state while rEAG and HCN1 remain α-helical without transitions to a π helical conformation over comparable timescales (Figure Figure 4 - Figure supplement 1B).

The π-helix conformation of hERG results in a rotation of the lower half of S6 away from the symmetry axis, enabling pore hydration and ion conduction. This is most evident in the position immediately preceding the hinge (F656 - hERG numbering) which faces inward towards the S6-S6 interface in the closed state of rEAG but rotates towards the S5-S6 interface in the open state of hERG (Figure 4A,B).

Furthermore, numerous CNG channels have been resolved in closed and open states and show similar gating movements and α to π helical transitions on opening to those noted for rEAG/hERG structures above (Zheng et al., 2020; Xue et al., 2021, 2022). This indicates that the structural mechanisms of pore gating observed in rEAG/hERG may be a conserved gating transition in the CNBD family of channels. Given the structural homology observed in the closed and open states in the CNBD family, we reasoned that a homology model of the HCN1 open pore using hERG as a template could provide valuable insight on channel gating.

In this model, S6 is twisted at the glycine hinge, rotating the preceding residue (V390) out of its pore-lining position and enabling hydration of the inner vestibule. This places V390 at the S5-S6 interface in contact with I302 and M305 in the open state model. We assessed the stability of this HCN1 open state model using a 1 μs-long equilibrium MD simulation. This model stayed open and hydrated over the full simulation, suggesting that our π-helical model for the HCN1 open state is stable (Figure 4D). A few ions were able to cross the gate, indicating a model compatible with a conductive state of the channel (Figure 4 - Figure supplement 2).
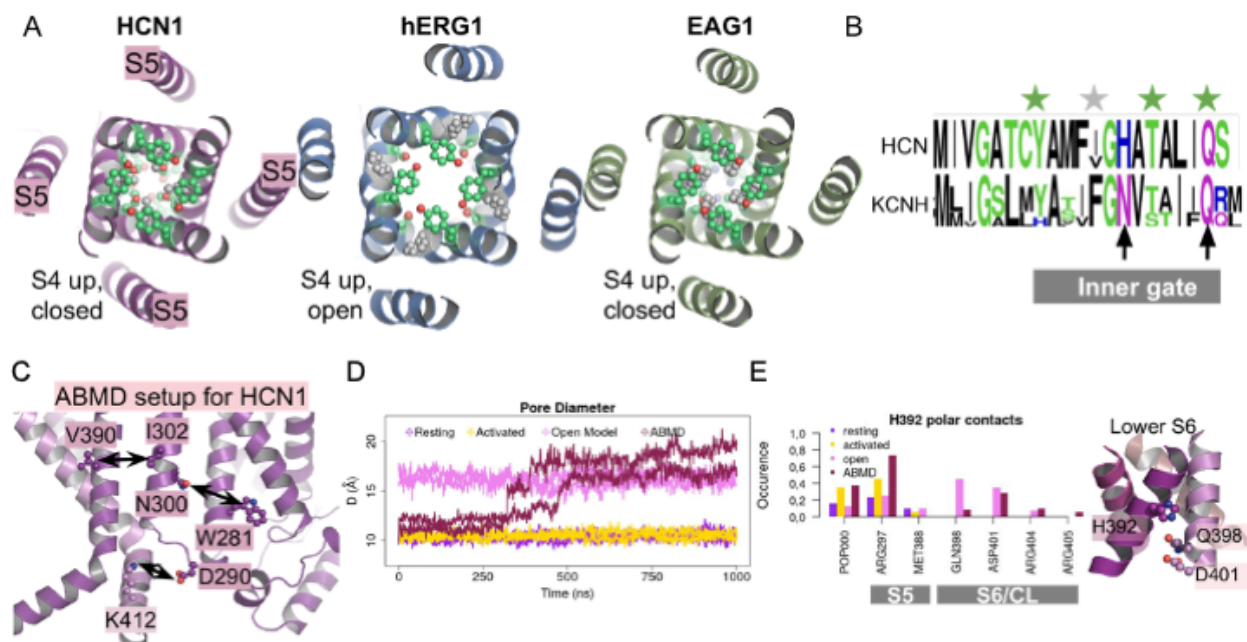
Figure 4: Pore opening of HCN1 shares features with pore opening in other KCNH channels.

(A) Top view of intracellular gate in the pore region of HCN1, hERG1 and EAG1. Hydrophilic and hydrophobic residues facing the pore lumen are highlighted in green and gray, respectively. (B) Sequence logo representation of S6 segment including the intracellular gate in HCN and KCNH channels. Residue positions in the intracellular gate region and facing the pore lumen in the HCN1 closed model are marked by stars. (C) Residues and distances used as collective variables in ABMD simulations are highlighted by ball and stick and black double arrows, respectively. (D) Inter-subunit distances between opposite V390 residues are represented as a function of time in the resting (purple), activated (yellow), open homology model (light purple) and ABMD (crimson) simulations. (E) Contact occurences of H392 in HCN1 are shown for the resting (purple), activated (yellow), open homology model (light purple) and ABMD (crimson) simulations. The inset on the right is showing the inner constriction of the lower S6 helices. H392 on one helix and adjacent Q398 and D401 are highlighted in ball and stick.
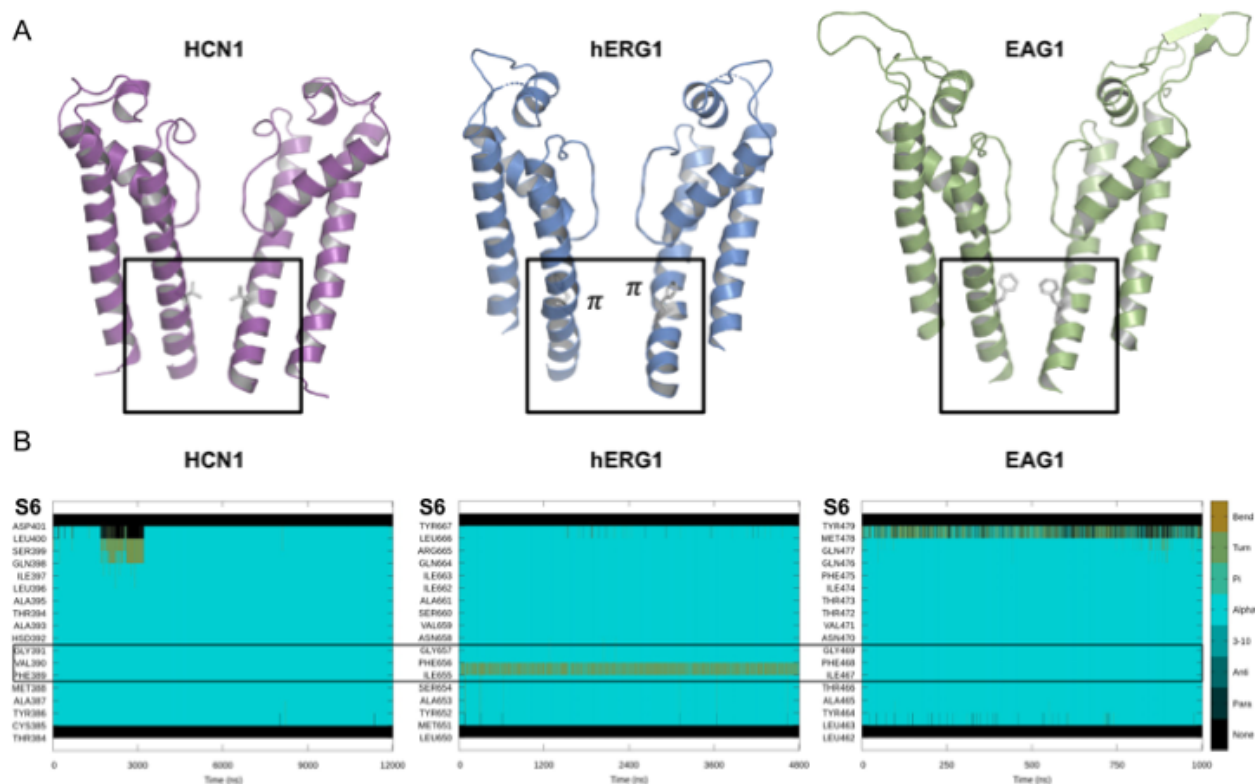
Figure 4 - Figure supplement 1: S6 deformation within the intracellular gate.

(A) Pore domains of cryo-EM structures of HCN1 (left - PDB ID 5U6P), hERG1 (middle - PDB ID 5AV2) and EAG1 (right - PDB ID 6PBY). For clarity only two opposing subunits are represented. Intracellular gate residues V390, F656 and F468 are highlighted as grey sticks in HCN1, hERG1 and EAG1, respectively. (B) Secondary structure evolution of S6 segment along MD simulations of HCN1(left), hERG1 (middle) and EAG1 (right). Black boxes point to the region around V390, F656 and F468 in HCN1, hERG1 and EAG1, respectively.
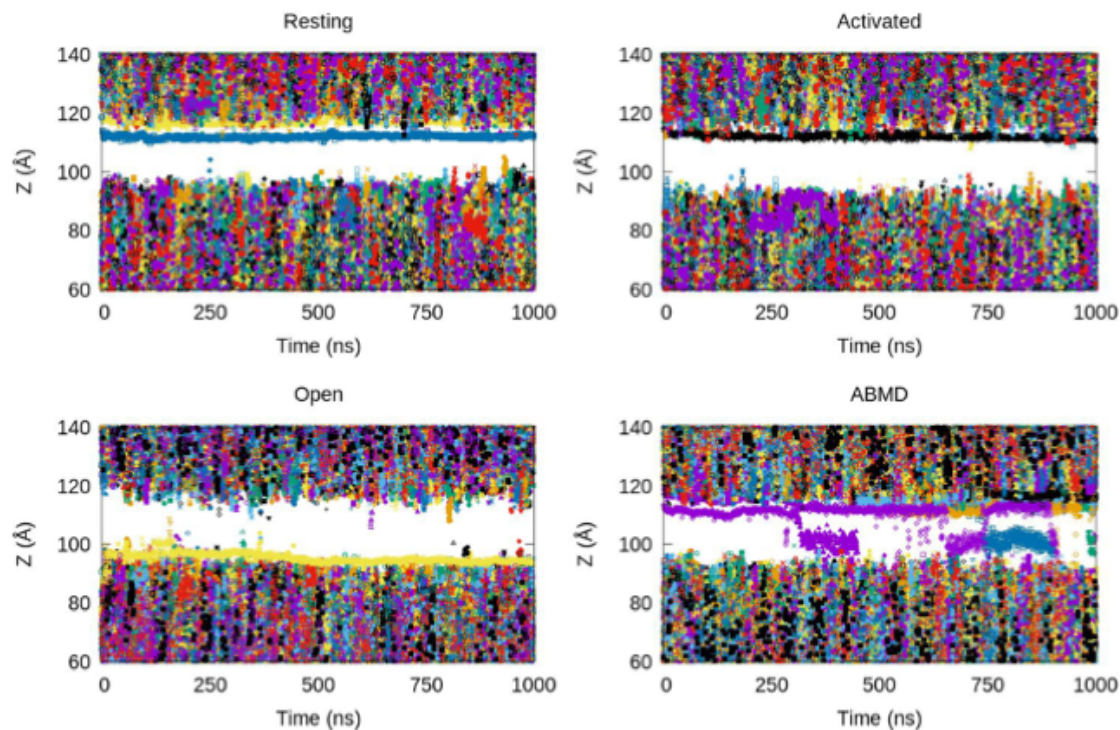
Figure 4 - Figure supplement 2: Potassium permeation along the HCN1 pore.

Positions of potassium ions along the Z-axis of the simulation box, each shown in a different symbol and color, as a function of the simulation time. The membrane is located between Z=~90 Å and Z=~120 Å. Data from four simulations are shown: resting and activated HCN1 structures equilibrium MD simulations, open HCN1 homology model equilibrium MD simulation and ABMD simulation of the transition between resting/closed and activated/open states.

Figure 4 - Figure supplement 3: Opening implies reinforced hydrophobic S6-S5 and weakened hydrophobic S6-S6 interfaces.
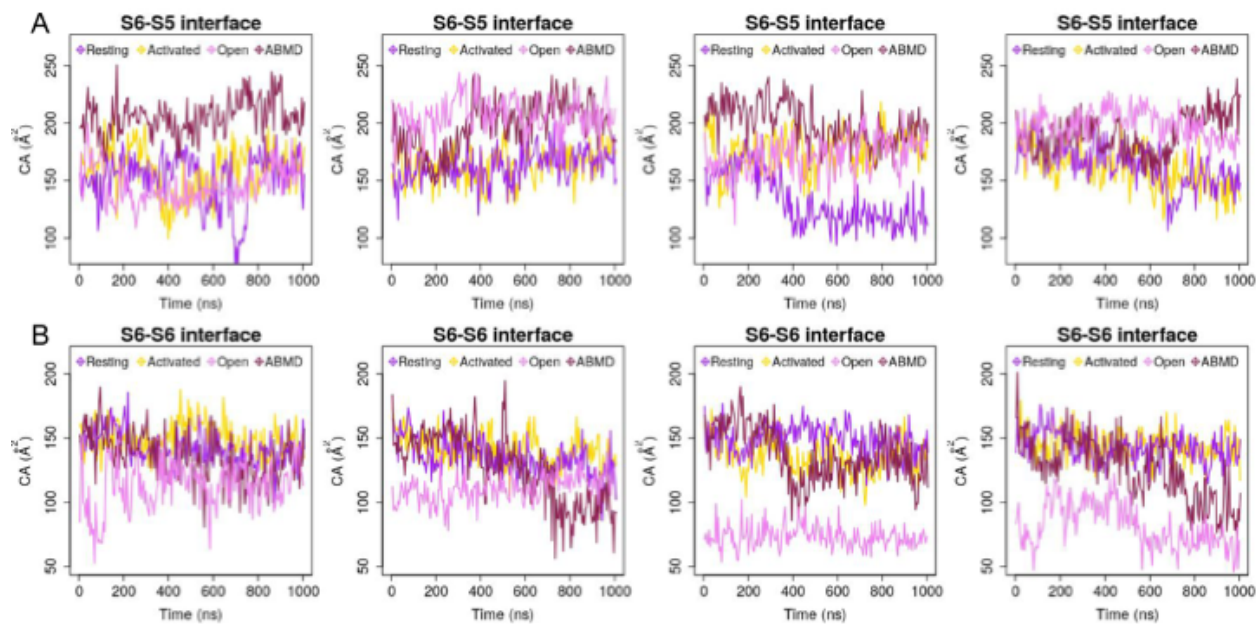
(A) Evolution of the contact areas between intra-subunit lower S5 and S6 as a function of time in each subunit in the resting (purple), activated (yellow) and homology open models (light violet) equilibrium simulations and in the ABMD simulation (dark violet red) starting from the resting state. (B) Evolution of the contact areas between adjacent (inter-subunit) lower S6 helices as a function of time in each subunit in the resting (purple), activated (yellow) and homology open models (light violet) equilibrium simulations and in the ABMD simulation (dark violet red) starting from the resting state.

Driving electromechanical coupling in enhanced sampling simulations

In the previous sections, we have identified several interactions that are likely involved in stabilizing the activated voltage sensor and/or open pore. The W281-N300 pair at the S4/S5 interface stabilizes the rotation of the C-terminus of S4 on activation. Interaction between D290-K412 on the S4-S5 linker and C-linker promotes the bending of S5 away from the resting conformation, loosening the packing against the closed state of S6. Finally, V390-I302 (on S6 and S5, respectively) interaction correlates with the rotation of the lower S6 at the glycine hinge and opening of the inner gate. Using these state-specific interactions as collective variables (CVs) in enhanced sampling MD simulations, we hypothesized that we could drive the electromechanical coupling process in a computationally accessible timescale.

Of the numerous available enhanced sampling techniques we opted for adiabatic bias MD (ABMD) simulations given the gentle nature of the biasing potential applied. ABMD simulations

allow thermal fluctuations to carry the system forward over energy barriers while only applying biasing potentials dampening movement in the backwards direction. We introduced these ratchet-like biases to encourage the formation of interactions between the three open-state specific contacts detailed above (V390-I302, N300-W281, and D290-K412) in a 1 microsecond ABMD simulation starting from the HCN1 resting state (Figure 4C).

During this simulation, we observed a rotation of the V390 side chain from a position facing the pore lumen to a position facing I302 on S5 (Movie 1). This event is coupled to an increase of the pore radius at the V390 position, an increased hydration of the pore intracellular gate (Figure 4D, Movie 2) and even enabled the conduction of several K+ ions (Figure 4 - Figure supplement 2). The rotation of V390 also induced other conformational changes in the C-terminus of S6: in particular, a contact between H392 and adjacent D401 formed at the end of the ABMD simulation, even though the formation of this contact was not explicitly encouraged in the biasing simulations. In addition, a contact between H392 and the pore lining Q398 (Figure 4B, black arrows) of adjacent subunits formed intermittently (Figure 4E). These contacts are also present in the open state homology model (Figure 4E). Interestingly, the equivalent hERG1 contacts N658-Q664 are stably formed in the open state channel under activating conditions. Thus, we suggest that H392-Q398 contact should be formed/maintained to induce pore widening and stabilize the open conformation in HCN1.

Energetic Basis for electromechanical coupling

Calculations of the intra subunit contact areas between S6 (from residue 386 to 401) and S5 (lower segment) showed an overall reinforcement of the hydrophobic contact area in the open model and ABMD simulations of HCN1 indicating that closure/opening are related to changes of interfaces between pore helices (Figure 4 - Figure supplement 3A). By contrast, the adjacent S6-S6 hydrophobic interfaces are more likely to be weakened suggesting that the enlargement of the pore radius requires an increased distance between S6 helices (Figure 4 - Figure supplement 3B).

The analysis of the interaction between lipid headgroups of the lower leaflet POPC lipids and the innermost S4/S5/S6 region revealed a state-dependent pattern (Figure 5A). Indeed, lipids tended to bind in two separate sites (sites A and B, Figure 5B,C), located on opposite sides of the S4/S5/S6 interface. In both of these sites, contacts with polar or charged residues were increased in the activated state relative to the resting one, and involved a larger number of lipids. Site B especially engaged VSD residues, including S4 gating charges. Site A, on the other hand, engaged in addition residues on S5 (R297) and on S6 (H392)

Interestingly, H392, pinpointed as crucial for pore gating above, is located in the middle of the sequence corresponding to the inner constriction on S6 and is highly conserved in the HCN family (Figure 4B). Its position at the lipid interface allows it to be flexible. Thus, this residue is capable of making contacts both with R297 on S5, and with a POPC headgroup from the lower bilayer leaflet (Figure 5), sometimes engaging in a ternary interaction with both binding partners. In fact, both the H392-R297 contact and their contact with lipids are reinforced in the activated state, confirming that these contacts are implicated in activation and opening (Figure 4E, 5). We hypothesize that these lipids play a particular role in coupling S5 and S6 in a way as to enable pore gating. Overall, these observations imply that activation and following opening of HCN1 are also driven by a combination of forces: one one hand, hydrophobic forces reinforce the intra-subunit S4/S5/S6 interface, while on the other, the positioning of lipid headgroups in contact with hydrophilic residues located at this interface also guides the positioning of lipid tails that contribute to the overall hydrophobic region.
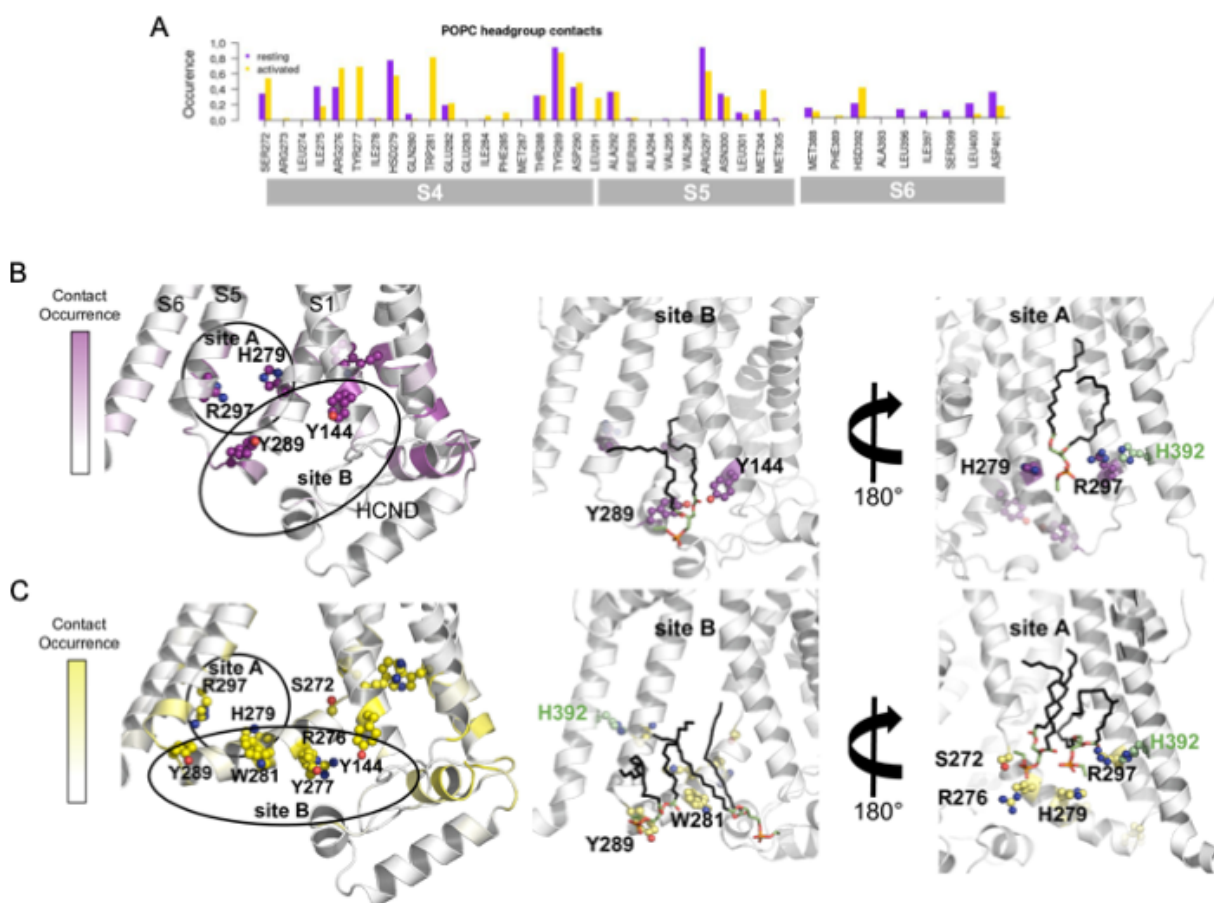

Figure 5: Interactions between the lower S4/S5/S6 region of HCN1 and the lipid headgroups are state-dependent.

(A) Contact area between lower S4/S5/S6 protein residues and lipid headgroups averaged over the 4 subunits and over the simulation time, in the resting (purple) and activated (yellow) states. (B) Residues from lower S1/S4/S5 in contacts with lipid headgroups for more than 50% of the simulation time in the resting HCN1 are highlighted in purple. Snapshot of POPC lipids (sticks) bound to lipid headgroup binding sites found in HCN1 resting state (C) Residues from lower S1/S4/S5 in contacts with lipid headgroups for more than 50% of the simulation time in the activated HCN1 are highlighted in yellow. Snapshot of POPC lipids (sticks) bound to lipid headgroup binding sites found in HCN1 activated state.

Discussion

The slow intrinsic gating and weak coupling between the VSD and pore presents a substantial challenge for characterizing the electromechanical coupling pathway in HCN channels with computational methods. While voltage sensor activation can be dramatically accelerated with an electric field, pore opening is only indirectly influenced through allosteric interaction via the electromechanical coupling pathway. Due to the weak coupling energy in HCN channels, the ability of the voltage sensors to expedite gating is much more limited than in strongly coupled VGICs such as Shaker. We have circumvented these limitations using state-specific contacts derived from equilibrium simulations on the existing models of HCN1 to drive the electromechanical coupling process using enhanced sampling. Integrating the results from these simulations enables us to propose a model for electromechanical coupling in HCN channels that builds upon and further refines current models of channel gating (Figure 6).

From the resting state of HCN1, hyperpolarization drives downward movement of the gating charges and helix-breakage at S272 and initiates a cascade of rearrangements of the hydrophobic interfaces between and within the VSD and pore. This hydrophobic "domino effect" starts when W281 is pulled out of a hydrophobic cavity formed by S1 and the HCN domain, enabling rotation of the lower S4 helix, driving formation of new VSD-pore contacts between W281 (S4) with V296 and N300 (S5). This two step-activation mechanism induces an increase of the hydrophobic interface between the lower S4, S5, and the surrounding lipid tails, thus reinforcing coupling between the VSD and pore as S4 activates. The increased S4/S5 coupling as S4 is displaced from the resting state results in a slight bending of S5 away from S6 and enables S6 to rotate radially away from the pore axis to maintain and even strengthen hydrophobic S5/S6 contacts. Rotation of S6 results in a π-helical deformation at a conserved glycine hinge and enables rotation of the hydrophobic V390 away from the ion permeation pathway to permit conduction through the open pore. The combined VSD activation and pore opening also allows a

more favorable accommodation of a lipid headgroup at the lower S4/S5/S6 interface (E282-R297-H392), which could be a crucial lipid modulation binding site.

A two-step mechanism for VSD activation was recently identified in spHCN using VCF and gating currents to track voltage sensor movement on the E356A (Wu et al., 2021). This mutant uncouples the primary gating charge movement from pore opening and reveals a secondary movement of the voltage sensor that correlates with channel opening. This secondary movement may correspond to either the bending or rotation of the lower S4 helix. However, our simulation of the structure of the Y289D uncoupling mutant would suggest that rotation of S4 alone can drive pore opening as the W281-N300 contact is formed but no bend is observed in S4. Furthermore, this model for an altered S4/S5 interface upon rotation of the lower S4 also explains how voltage sensor movement can still be coupled to pore gating in channels lacking a covalent linkage between the S4 and S5 (Flynn and Zagotta, 2018).

Based on their work with such split channels and extensive mutagenesis, Flynn and Zagotta suggested that the lower S4-S5 interface plays a critical role in stabilizing the closed state of the pore (Flynn and Zagotta, 2018). Activation of the VSD relieves this inhibitory effect and enables the more favorable open state of S6. Our simulations reveal that pore opening involves a tradeoff between a strengthening of the S5/S6 interface at the expense of a weakening of the S6-S6 interface. While this stabilization of the S5/S6 interface upon opening is seemingly at odds with the model of Flynn and Zagotta, this difference can be reconciled by examining the mechanism of S6 gating. Voltage sensor activation displaces the lower S4/S5 interface away from the closed conformation of S6, enabling dilation of the S6 helices via rotation around a π-helix at a conserved glycine hinge. Thus the resting conformation of S5 sterically hinders this outward and rotating movement of S6, in line with previous studies (Flynn and Zagotta, 2018).

The π-helical model of the open state of S6 from our simulations is slightly different from the open conformation of HCN4 observed in cryoEM (Saponaro et al., 2021, 4). In the HCN4 open conformation, the equivalent of V390 (I511) is rotated slightly but does not induce formation of a π-helix. Although it is possible that the difference observed between the HCN4 cryoEM structure and our simulations of HCN1 represent differences between isoforms, we propose this difference stems from the different functional states these models represent. The HCN4 structure was solved in the resting VSD conformation, thus corresponds to the resting-open state or the "instantaneous" open state of HCN channels. The instantaneous open state is pharmacologically distinguishable from the activated-open state suggesting structural differences in the pore (Proenza et al., 2002). Furthermore, the open state of numerous CNG channels also adopt a similar π-helix in S6,

suggesting that this is a conserved mechanism of pore gating in the CNBD family (Zheng et al., 2020; Xue et al., 2021, 2022).

The prevalence of state-dependent lipid interactions favoring the activated VSD and open pore highlight a potential role in electromechanical coupling. Saponaro *et al*. also report state-dependent lipid binding at the S4/S5/S6 interface in their closed and open structures of HCN4, though they observe lipid density only in the resting-closed state and not in the resting-open state (Saponaro et al., 2021). A similar lipid density was observed in the resting-closed structure of the hyperpolarization-activated plant channel KAT1 (Clark et al., 2020). Here, we used a simple model bilayer of POPC whereas the copurified lipid in the HCN4 and KAT1 structures could not be identified by the density. Examining the state-dependence of lipid binding at the VSD-pore interface in more complex environments will be crucial for improving our understanding of lipid regulation of HCN channel function.
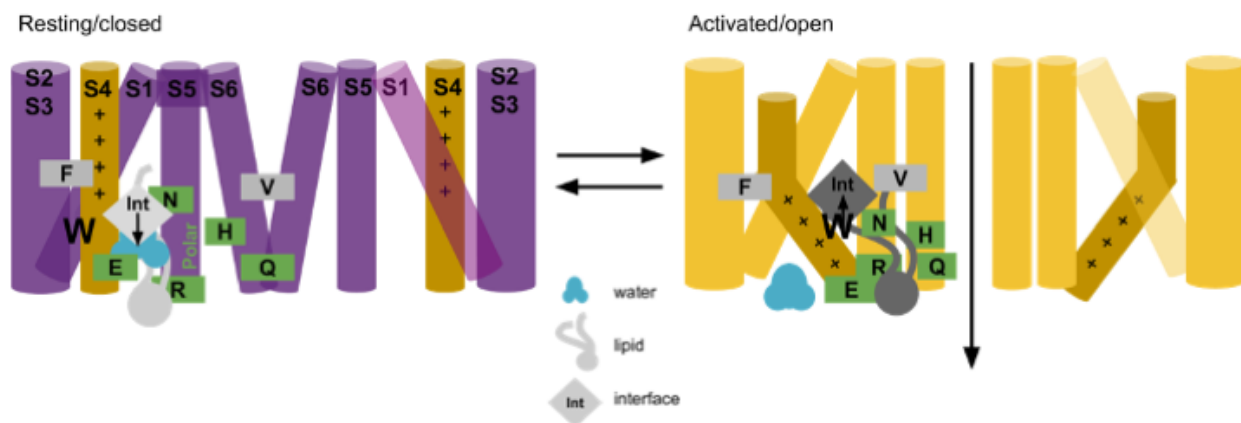

Figure 6: Hydrophobic domino-effect model of HC1 gating upon activation.

Hyperpolarization triggers the downward and breaking movement of S4 initiates a cascade of rearrangements of the hydrophobic interfaces between and within the VSD and pore. First, W281 is pulled out of a S1/HCND hydrophobic cavity leading the lower S4 helix to rotate and form of new contacts with S5. This is accompanied by an increase of the hydrophobic interface between the lower S4, S5, and the surrounding lipid tails. These interactions result in a slight bending of S5 away from S6 and enables rotation of S6 away from the pore axis resulting in a rotation of V390 away and opening of a conductive hydrophilic pathway along the pore axis. The combined VSD activation and pore opening allows accommodation of a lipid headgroup at the lower S4/S5/S6 interface (E282-R297-H392).

Materials and methods

Protein models

Cryo-EM structures of the resting (5U6P), intermediate (mutant Y289D, 6UQG) and the activated (6UQF) states of HCN1 were used as initial snapshots for MD simulations (Lee and MacKinnon, 2019, 2017). Cyclic nucleotides solved in these structures were kept within each CNBD. A WT-model without the HCN domain (without residues 94 to 139) was also built using the HCN1 resting state (5U6P) as a starting model. In addition, KCNH cryo-EM structures, hERG1 (5AV2) and EAG1 (6PBY), from which we removed the PAS domain and other cofactors (calmodulin), were extracted as starting points for MD simulations. Finally, a homology model of the open pore of HCN1 was also built using iTasser (Roy et al., 2010), using the hERG1 3D structure (5AV2) as a template.

System building

The different channel models were prepared using the CHARMM-GUI server (Jo et al., 2008; Lee et al., 2015). Each channel was embedded in a 1-palmytoyl-2-oleoyl-phosphatidyl-choline (POPC) bilayer (150x150 Å) and solvated in a 150 mM KCl solution. The CHARMM36 force field was used for the protein, lipids and ions, and the TIP3P model for water(Klauda et al., 2010; Huang and MacKerell, 2013). The CgenFF module was used to parametrize cAMP molecules solved in HCN1 structures (Vanommeslaeghe et al., 2010).

Molecular dynamics simulations

Minimization, equilibration and production steps were performed on the Beskow-SNIC / Piz-daint supercomputers using, respectively, Gromacs 2019.3 and 2020.3 (Abraham et al., 2015; Lindahl et al., 2021) . The standard CHARMM-GUI inputs were used for the minimization and equilibration of the systems. During these steps, harmonic restraints applied to the protein heavy atoms and the lipid heads and were gradually released during 1.2 ns. The production dynamics were then performed in the NPT ensemble without any restraints. Hyperpolarized or depolarized conditions were applied by imposing, respectively, a positive or negative electric field in the form of an external force acting on all charged particles of the system. Nose-Hoover thermostat (Nosé, 1984, 199) and Parrinello-Rahman barostat (Parrinello and Rahman, 1981) used to keep the temperature and the pressure constant at 310 K and 1 bar. Periodic boundary conditions were used and the particle mesh ewald algorithm (Darden et al., 1993) was applied to treat long-range electrostatic interactions. A switching function was applied between 10 and 12 Å for the non-

bonded interactions. LINCS (Hess et al., 1997) was applied to constrain the bond lengths involving hydrogen atoms. The integration timestep was set to 2 fs and the overall lengths of the trajectories are 1 µs.

Longer simulations of equilibrium resting/closed HCN1, open hERG and closed EAG. were performed using the Anton2 supercomputer (Shaw et al., 2014). These simulations were performed using standard CHARMM36 parameters in the NVT ensemble to avoid altering the applied electric field. The temperature was kept at 310 K using the Nose-Hoover thermostat. The multigrator approach was used for temperature and semi-isotropic pressure coupling. Long range electrostatic interactions were handled using the u-series algorithm implemented in Anton2 (Lippert et al., 2013). The timestep was kept to 2 fs. All simulated structures and simulation details are listed in Table 1.

Table 1: Table summary of the MD simulations carried out in this work. Cryo-EM structures (1rst column, pdb code in brackets) were simulated under different conditions (2nd column, including presence/absence of specific domains/binding partners, under external electric field [EF] or not). The total simulation time is provided in the 3rd column.

Structure	Conditions	Time (ns)
HCN1 resting with cAMP (5U6P)	no EF	1000
HCN1 intermediate with cAMP (6UQG)	no EF	1000
HCN1 activated closed with cAMP (6UQF)	no EF	1000
HCN1 resting with cAMP (5U6P)	without HCN domain + EF (-1 V)	750
HCN1 resting with cAMP (5U6P)	EF (-1 V)	1000
HCN1 resting with cAMP (5U6P)	EF (-550 mV)	12000
hERG activated open (5VA2)	without PAS + EF (+750 mV)	4800
EAG activated closed (6PBY)	without (calmodulin+PAS) + EF (+1 V)	1000
HCN1 Open homology model	No EF	1000
HCN1 resting with cAMP (5U6P)	**ABMD** + EF (-)	1000

Enhanced sampling MD simulations with ABMD

Adiabatic bias molecular dynamics (ABMD) simulations were carried out using gromacs and the same simulation conditions described above (Marchi and Ballone, 1999). In this method, a

ratchet-like biasing harmonic potential is added, encouraging further exploration of the collective variable (CV) space. In these simulations, Plumed2.5 (Tribello et al., 2014) was called along the MD production, to apply a bias on 3 Collective Variables (CVs), namely the distance between the center of mass of W281-N300, D290-K412 and V390-I302 residue pairs. The distance target T0 was set to 4.0 Å and the bias force constant KAPPA equal to 4000.0 kJ/mol for each CV.

MD simulations Analysis

Contact analysis

The contacts between helices were analyzed by VLDM (Voronoi Laguerre Delaunay for Macromolecules) (Esque et al., 2010). VLDM relies on a tessellation method, that is, a partition of space into a collection of polyhedra filling space without overlaps or gaps. Delaunay tessellation and its Laguerre dual is performed using a set of heavy atom cartesian coordinates and a weight that depends on the van der Waals radius of the atom, determined using the CHARMM36 force field. A contact occurs whenever two atoms share a common face in the tessellation. The interface between molecular groups is quantified by their polygonal surface area. The type of contacts in the interface determines the nature of the interface: hydrophobic contacts correspond to contacts between carbon atoms exclusively while electrostatic contacts involve N, O, S and P atoms; hydrogen bonds and salt bridges both belong to this category.

MSA and sequence logo representation

A first Multiple Sequence Alignment (MSA) was obtained by applying MAFFT algorithm (Katoh et al., 2002) on a small set of sequences of human non domain swapped HCN, KCNH and CNG channels (HCN1-4, hERG1-4, hEAG1-2, ELK1-2, CNGA1-4) and of non-human channel sequences for which 3D structures are available (TAX4 and KAT1) or for which extensive experimental data has been reported (spHCN). This first MSA was manually annotated and used as input for HMMER search (Finn et al., 2011), which yielded an ensemble of 9 478 homologous channels. Hierarchical clustering (3 steps runs) using cd-hit algorithm allowed to separate this large set of sequences into 4 clusters (Li and Godzik, 2006): the HCN-, KCNH-, CNGA-, KAT-containing groups. MSA of these clusters were generated with MAFFT and manually curated/annotated according to the initial MSA and then converted into a sequence logo representation by family/cluster using WebLogo webserver (Crooks et al., 2004).

Visualization and analysis

Positions and distances were calculated using in-house tcl scripts for VMD. The S4 bending angle, which corresponds to the angle formed between the axis of upper S4 (254-272) and that of lower S4 (272-289), was calculated along MD trajectories using PLUMED v2.5. MD simulation trajectories were visualized using VMD (Humphrey et al., 1996) and PyMOL. Positions, distances, angles and contacts graphs were all generated using R v3.6.1 or gnuplot v5.0.

Cell Culture and transient expression

293T (ATCC, CRL-3216) were cultured in DMEM (Gibco, 11965-084) supplemented with 10 % FBS (Gibco, 26140-079) and 2 mM L-glutamine (Corning, 25005CI). The cells were kept at 37 °C and 8% CO_2 in a humidified incubator and were split every three days. For transfections, the cells were plated in a 12.5 cm^2 dish and were transfected at 60% confluency with 0.8 µg DNA using TransIT-293 (Mirus, MIR2700). We used a GFP-tagged and C-terminally truncated human HCN1 construct which was cloned into a pEG plasmid as previously reported by Lou & MacKinnon (2017). Herein, we refer to this construct as HCN1-EM. For the double cysteine mutant, residues D290 and K412 were substituted with a cysteine each. The sequence of the construct was confirmed by DNA-sequencing. HCN1-EM or D290C-K412C channels were expressed in 293T cells for 24h and were plated at low density onto poly-L-lysine-coated 35 mm dishes before electrophysiological evaluation.

Electrophysiology and data analysis

Macroscopic currents were recorded in whole-cell voltage-clamp configuration using an Axopatch 200b amplifier (Molecular Devices, USA). Signals were lowpass filtered at 2 kHz by a 4-pole Bessel filter and acquired at a sampling rate of 10 kHz using a Digidata 1440A (Molecular Devices, USA). Data analysis was carried out in Clampfit 10 (Molecular Devices, USA) and Origin (Origin Lab Corporation, USA). The bath solution contained 130 mM NaCl, 10 mM KCl, 1.8 mM $CaCl_2$, 0.5 mM $MgCl_2$, 5 mM HEPES, pH = 7.4 NaOH. The pipette resistance was in the range of 1-2 MΩ, using a pipette solution consisting of 130 mM KCl, 10 mM NaCl, 0.5 mM $MgCl_2$, 2 mM Mg-ATP and 5 mM HEPES, pH=7.2 KOH. For the cysteine-corsslinking experiment, we added 100 µM cadmium to the pipette solution. To allow for equilibration of the cytosol with the pipette solution, we waited at least two minutes after breaking into the cells.

HCN1-EM expressing cells were clamped to a holding potential of -30 mV. Substitution of residues D290 and K412 with cysteins resulted in a shift of the half-maximal activation to depolarized potentials. The cells were therefore clamped to a holding potential of +60 mV, a potential at which the channels were in the resting state. To assess the voltage-dependence of

activation, we used a two-pulse protocol in which the channels were preconditioned to voltages in the range of +60 mV (HCN1-D290C-K412C) to -140 mV with -20 mV increments, before tail currents at a test pulse of -140 mV, a potential of maximal channel activation, were recorded. The inter-sweep time was set to 30 s, to ensure complete deactivation before the next pre-condition pulse was applied. Tail currents recorded herein are transient currents, where the initial current resembles an ensemble current of channels activated during the pre-conditioning pulse, and which increases during the test pulse until the maximal open probability is reached. Thus, the initial current of the tail current plotted as a function of voltage can be used to obtain channel activation. The activation curve was normalized and fitted with a single Boltzmann function: $y = (A_1 - A_0) / (1 + \exp((V - V_{0.5}) / k)) + A_0$, where A_0 and A_1 are the minimum and maximum tail current, $V_{0.5}$ is the potential of half maximal channel activation, V is the membrane potential and k is the slope factor. In HCN1-D290C-K412C expressing cells, we observed a high basal activity. To assess if the basal activity was a result of leak current or due to increased channel activity, we performed cesium-blocking experiments, in which we perfused the cells with 3 mM cesium-containing extracellular solution. Cesium is a potassium channel blocker and inhibits HCN1-mediated currents too. Thus, the remaining current seen during cesium application can be used to assess the leak current, that occurs because of poor seal resistance or through cesium-resistant channels. Subtraction of the leak current from the tail current were used to provide an estimate of the basal channel activity of HCN1. Data are given as mean ± SEM. for the indicated number of experiments (n).

References

Abraham, M.J., T. Murtola, R. Schulz, S. Páll, J.C. Smith, B. Hess, and E. Lindahl. 2015. GROMACS: High performance molecular simulations through multi-level parallelism from laptops to supercomputers. *SoftwareX*. 1–2:19–25. doi:10.1016/j.softx.2015.06.001.

Altomare, C., A. Bucchi, E. Camatini, M. Baruscotti, C. Viscomi, A. Moroni, and D. DiFrancesco. 2001. Integrated Allosteric Model of Voltage Gating of Hcn Channels. *J. Gen. Physiol.* 117:519–532. doi:10.1085/jgp.117.6.519.

Bell, D.C., H. Yao, R.C. Saenger, J.H. Riley, and S.A. Siegelbaum. 2004. Changes in Local S4 Environment Provide a Voltage-sensing Mechanism for Mammalian Hyperpolarization–activated HCN Channels. *J. Gen. Physiol.* 123:5.

Benarroch, E.E. 2013. HCN channels: Function and clinical implications. *Neurology*. 80:304–310. doi:10.1212/WNL.0b013e31827dec42.

Biel, M., C. Wahl-Schott, S. Michalakis, and X. Zong. 2009. Hyperpolarization-activated cation channels: from genes to function. *Physiol. Rev.* 89:847–885. doi:10.1152/physrev.00029.2008.

Bleakley, L.E., C.E. McKenzie, M.S. Soh, I.C. Forster, P. Pinares-Garcia, A. Sedo, A. Kathirvel, L. Churilov, N. Jancovski, S. Maljevic, S.F. Berkovic, I.E. Scheffer, S. Petrou, B. Santoro, and C.A. Reid. 2021. Cation leak underlies neuronal excitability in an HCN1 developmental and epileptic encephalopathy. *Brain J. Neurol.* 144:2060–2073. doi:10.1093/brain/awab145.

Blunck, R., and Z. Batulan. 2012. Mechanism of Electromechanical Coupling in Voltage-Gated Potassium Channels. *Front. Pharmacol.* 3.

Brown, H.F., D. Difrancesco, and S.J. Noble. 1979. How does adrenaline accelerate the heart? *Nature*. 280:235–236. doi:10.1038/280235a0.

Clark, M.D., G.F. Contreras, R. Shen, and E. Perozo. 2020. Electromechanical coupling in the hyperpolarization-activated K + channel KAT1. *Nature*. 583:145–149. doi:10.1038/s41586-020-2335-4.

Crooks, G.E., G. Hon, J.-M. Chandonia, and S.E. Brenner. 2004. WebLogo: a sequence logo generator. *Genome Res.* 14:1188–1190. doi:10.1101/gr.849004.

Dai, G., and W.N. Zagotta. 2017. Molecular mechanism of voltage-dependent potentiation of KCNH potassium channels. *eLife*. 6:e26355. doi:10.7554/eLife.26355.

Darden, T., D. York, and L. Pedersen. 1993. Particle Mesh Ewald - an Nlog(N) method for ewald sums in large systems. *J Chem Phys*. 98:10089–10092.

DiFrancesco, J.C., B. Castellotti, R. Milanesi, F. Ragona, E. Freri, L. Canafoglia, S. Franceschetti, C. Ferrarese, S. Magri, F. Taroni, C. Costa, A. Labate, A. Gambardella, R. Solazzi, A. Binda, I. Rivolta, G. Di Gennaro, S. Casciato, L. D'Incerti, A. Barbuti, D. DiFrancesco, T. Granata, and C. Gellera. 2019. HCN ion channels and accessory proteins in epilepsy: genetic analysis of a large cohort of patients and review of the literature. *Epilepsy Res.* 153:49–58. doi:10.1016/j.eplepsyres.2019.04.004.

DiFrancesco, J.C., and D. DiFrancesco. 2015. Dysfunctional HCN ion channels in neurological diseases. *Front. Cell. Neurosci.* 9.

Esque, J., C. Oguey, and A.G. de Brevern. 2010. A Novel Evaluation of Residue and Protein Volumes by Means of Laguerre Tessellation. *J. Chem. Inf. Model.* 50:947–960. doi:10.1021/ci9004892.

Finn, R.D., J. Clements, and S.R. Eddy. 2011. HMMER web server: interactive sequence similarity searching. *Nucleic Acids Res.* 39:W29-37. doi:10.1093/nar/gkr367.

Flynn, G.E., and W.N. Zagotta. 2018. Insights into the molecular mechanism for hyperpolarization-dependent activation of HCN channels. *Proc. Natl. Acad. Sci.* 115:E8086–E8095. doi:10.1073/pnas.1805596115.

Hess, B., H. Bekker, H.J.C. Berendsen, and J.G.E.M. Fraaije. 1997. LINCS: A linear constraint solver for molecular simulations. *J. Comput. Chem.* 18:1463–1472. doi:10.1002/(SICI)1096-987X(199709)18:12<1463::AID-JCC4>3.0.CO;2-H.

Huang, J., and A.D. MacKerell. 2013. CHARMM36 all-atom additive protein force field: Validation based on comparison to NMR data. *J. Comput. Chem.* 34:2135–2145. doi:10.1002/jcc.23354.

Humphrey, W., A. Dalke, and K. Schulten. 1996. VMD - Visual Molecular Dynamics. *J Molec Graph.* 14:33–38.

James, Z.M., and W.N. Zagotta. 2018. Structural insights into the mechanisms of CNBD channel function. *J. Gen. Physiol.* 150:225–244. doi:10.1085/jgp.201711898.

Jo, S., T. Kim, V.G. Iyer, and W. Im. 2008. CHARMM-GUI: A web-based graphical user interface for CHARMM. *J. Comput. Chem.* 29:1859–1865.

Kasimova, M.A., D. Tewari, J.B. Cowgill, W.C. Ursuleaz, J.L. Lin, L. Delemotte, and B. Chanda. 2019. Helix breaking transition in the S4 of HCN channel is critical for hyperpolarization-dependent gating. *eLife*. 8:e53400. doi:10.7554/eLife.53400.

Katoh, K., K. Misawa, K. Kuma, and T. Miyata. 2002. MAFFT: a novel method for rapid multiple sequence alignment based on fast Fourier transform. *Nucleic Acids Res.* 30:3059–3066. doi:10.1093/nar/gkf436.

Klauda, J.B., R.M. Venable, J.A. Freites, J.W. O'Connor, D.J. Tobias, C. Mondragon-Ramirez, I. Vorobyov, A.D. MacKerell, and R.W. Pastor. 2010. Update of the CHARMM All-Atom Additive Force Field for Lipids: Validation on Six Lipid Types. *J Phys Chem B.* 114:7830–7843. doi:10.1021/jp101759q.

Kusch, J., C. Biskup, S. Thon, E. Schulz, V. Nache, T. Zimmer, F. Schwede, and K. Benndorf. 2010. Interdependence of receptor activation and ligand binding in HCN2 pacemaker channels. *Neuron*. 67:75–85. doi:10.1016/j.neuron.2010.05.022.

Lee, C.-H., and R. MacKinnon. 2017. Structures of the Human HCN1 Hyperpolarization-Activated Channel. *Cell*. 168:111-120.e11. doi:10.1016/j.cell.2016.12.023.

Lee, C.-H., and R. MacKinnon. 2019. Voltage Sensor Movements during Hyperpolarization in the HCN Channel. *Cell*. 179:1582-1589.e7. doi:10.1016/j.cell.2019.11.006.

Lee, J., X. Cheng, J.M. Swails, M.S. Yeom, P.K. Eastman, J.A. Lemkul, S. Wei, J. Buckner, J.C. Jeong, Y. Qi, and others. 2015. CHARMM-GUI input generator for NAMD, GROMACS, AMBER, OpenMM, and CHARMM/OpenMM simulations using the CHARMM36 additive force field. *J. Chem. Theory Comput.* 12:405–413.

Li, M., X. Zhou, S. Wang, I. Michailidis, Y. Gong, D. Su, H. Li, X. Li, and J. Yang. 2017. Structure of a eukaryotic cyclic-nucleotide-gated channel. *Nature*. 542:60–65. doi:10.1038/nature20819.

Li, W., and A. Godzik. 2006. Cd-hit: a fast program for clustering and comparing large sets of protein or nucleotide sequences. *Bioinforma. Oxf. Engl.* 22:1658–1659. doi:10.1093/bioinformatics/btl158.

Lindahl, Abraham, Hess, and van der Spoel. 2021. GROMACS 2021.2 Manual. doi:10.5281/zenodo.4723561.

Lippert, R.A., C. Predescu, D.J. Ierardi, K.M. Mackenzie, M.P. Eastwood, R.O. Dror, and D.E. Shaw. 2013. Accurate and efficient integration for molecular dynamics simulations at constant temperature and pressure. *J. Chem. Phys.* 139:164106. doi:10.1063/1.4825247.

Long, B.S., E.B. Campbell, and R. MacKinnon. 2005. Crystal structure of a mammalian voltage-dependent Shaker family K+ channel. *Science*. 309:897–903.

Lu, Z., A.M. Klem, and Y. Ramu. 2001. Ion conduction pore is conserved among potassium channels. *Nature*. 413:809–813. doi:10.1038/35101535.

Männikkö, R., F. Elinder, and H.P. Larsson. 2002. Voltage-sensing mechanism is conserved among ion channels gated by opposite voltages. *Nature*. 419:837–841. doi:10.1038/nature01038.

Marchi, M., and P. Ballone. 1999. Adiabatic bias molecular dynamics: A method to navigate the conformational space of complex molecular systems. *J. Chem. Phys.* 110:3697–3702. doi:10.1063/1.478259.

Nosé, S. 1984. A unified formulation of the constant temperature molecular dynamics methods. *J Chem Phys*. 81:511–519.

Oyrer, J., L.E. Bleakley, K.L. Richards, S. Maljevic, A.M. Phillips, S. Petrou, C.J. Nowell, and C.A. Reid. 2019. Using a Multiplex Nucleic Acid in situ Hybridization Technique to Determine HCN4 mRNA Expression in the Adult Rodent Brain. *Front. Mol. Neurosci.* 12.

Parrinello, M., and A. Rahman. 1981. Polymorphic transitions in single crystals: A new molecular dynamics method. *J. Appl. Phys.* 52:7182–7190. doi:10.1063/1.328693.

Proenza, C., D. Angoli, E. Agranovich, V. Macri, and E.A. Accili. 2002. Pacemaker channels produce an instantaneous current. *J. Biol. Chem.* 277:5101–5109. doi:10.1074/jbc.M106974200.

Ramentol, R., M.E. Perez, and H.P. Larsson. 2020. Gating mechanism of hyperpolarization-activated HCN pacemaker channels. *Nat. Commun.* 11:1419. doi:10.1038/s41467-020-15233-9.

Rothberg, B.S., K.S. Shin, and G. Yellen. 2003. Movements near the Gate of a Hyperpolarization-activated Cation Channel. *J. Gen. Physiol.* 122:501–510. doi:10.1085/jgp.200308928.

Roy, A., A. Kucukural, and Y. Zhang. 2010. I-TASSER: a unified platform for automated protein structure and function prediction. *Nat. Protoc.* 5:725–738. doi:10.1038/nprot.2010.5.

Ryu, S., and G. Yellen. 2012. Charge movement in gating-locked HCN channels reveals weak coupling of voltage sensors and gate. *J. Gen. Physiol.* 140:469–479. doi:10.1085/jgp.201210850.

Santoro, B., D.T. Liu, H. Yao, D. Bartsch, E.R. Kandel, S.A. Siegelbaum, and G.R. Tibbs. 1998. Identification of a Gene Encoding a Hyperpolarization-Activated Pacemaker Channel of Brain. *Cell*. 93:717–729. doi:10.1016/S0092-8674(00)81434-8.

Saponaro, A., D. Bauer, M.H. Giese, P. Swuec, A. Porro, F. Gasparri, A.S. Sharifzadeh, A. Chaves-Sanjuan, L. Alberio, G. Parisi, G. Cerutti, O.B. Clarke, K. Hamacher, H.M. Colecraft, F. Mancia, W.A. Hendrickson, S.A. Siegelbaum, D. DiFrancesco, M. Bolognesi, G. Thiel, B. Santoro, and A. Moroni. 2021. Gating movements and ion permeation in HCN4 pacemaker channels. *Mol. Cell*. 81:2929-2943.e6. doi:10.1016/j.molcel.2021.05.033.

Tanguay, J., K.M. Callahan, and N. D'Avanzo. 2019. Characterization of drug binding within the HCN1 channel pore. *Sci. Rep.* 9:465. doi:10.1038/s41598-018-37116-2.

Tribello, G.A., M. Bonomi, D. Branduardi, C. Camilloni, and G. Bussi. 2014. PLUMED 2: New feathers for an old bird. *Comput. Phys. Commun.* 185:604–613. doi:10.1016/j.cpc.2013.09.018.

Vanommeslaeghe, K., E. Hatcher, C. Acharya, S. Kundu, S. Zhong, J. Shim, E. Darian, O. Guvench, P. Lopes, I. Vorobyov, and A.D. Mackerell. 2010. CHARMM general force field: A force field for drug-like molecules compatible with the CHARMM all-atom additive biological force fields. *J. Comput. Chem.* 31:671–690. doi:10.1002/jcc.21367.

Wang, W., and R. MacKinnon. 2017. Cryo-EM Structure of the Open Human Ether-à-go-go-Related K+ Channel hERG. *Cell*. 169:422-430.e10. doi:10.1016/j.cell.2017.03.048.

Whicher, J.R., and R. MacKinnon. 2016. Structure of the voltage-gated K+ channel Eag1 reveals an alternative voltage sensing mechanism. *Science*. 353:664–669. doi:10.1126/science.aaf8070.

Wu, S., Z.V. Vysotskaya, X. Xu, C. Xie, Q. Liu, and L. Zhou. 2011. State-Dependent cAMP Binding to Functioning HCN Channels Studied by Patch-Clamp Fluorometry. *Biophys. J.* 100:1226–1232. doi:10.1016/j.bpj.2011.01.034.

Wu, X., R. Ramentol, M.E. Perez, S.Y. Noskov, and H.P. Larsson. 2021. A second S4 movement opens hyperpolarization-activated HCN channels. *Proc. Natl. Acad. Sci.* 118:e2102036118. doi:10.1073/pnas.2102036118.

Xue, J., Y. Han, W. Zeng, and Y. Jiang. 2022. Structural mechanisms of assembly, permeation, gating, and pharmacology of native human rod CNG channel. *Neuron*. 110:86-95.e5. doi:10.1016/j.neuron.2021.10.006.

Xue, J., Y. Han, W. Zeng, Y. Wang, and Y. Jiang. 2021. Structural mechanisms of gating and selectivity of human rod CNGA1 channel. *Neuron*. 109:1302-1313.e4. doi:10.1016/j.neuron.2021.02.007.

Zheng, X., Z. Fu, D. Su, Y. Zhang, M. Li, Y. Pan, H. Li, S. Li, R.A. Grassucci, Z. Ren, Z. Hu, X. Li, M. Zhou, G. Li, J. Frank, and J. Yang. 2020. Mechanism of ligand activation of a eukaryotic cyclic nucleotide−gated channel. *Nat. Struct. Mol. Biol.* 27:625–634. doi:10.1038/s41594-020-0433-5.